Stability Region Assessment With Mechanism-Data Driven Equivalent Impedance for Wind Power Plant

Shiyao Qin, Peng Wang, *Member, IEEE*, Shaolin Li, Haoran Zhao, *Senior Member, IEEE*, Jinlong Wang, and Jia Luo

***Abstract*—Online identification of the stability region for the wind power plant (WPP) equipped with permanent magnet synchronous generators encounters two challenges: calculating high-order impedance and estimating the stability boundary of multiple parameters. To address these challenges, the mechanism-data-driven equivalent impedance for each branch of the WPP is developed, and the high-dimensional stability region boundary is established with a machine learning-based algorithm. In mechanism-driven modeling, the aggregated impedance is derived using parallel calculation. In data-driven modeling, different key parameters in wide frequency bands are modified to ensure the accuracy of the equivalent impedance. The equivalent impedance derived through the mechanism-data-driven approach deviates from the detailed impedance within $\pm 1\%$. Regarding the stability region estimation, the fuzzy support vector machine is applied. To improve the speed of the online training of the stability region, the weighted Mahalanobis distance is employed to distinguish the importance of stability index samples. In validation, the stability regions of the power of the WPP are established. The impacts of the static var generator (SVG) on the stability performance are analyzed, and regulating the reactive power of the SVG can enhance small-signal stability. The stability region estimation and enhancement are verified through time-domain simulations and experiments in a controller-hardware-in-loop platform.**

***Index Terms*—Equivalent impedance, machine learning, small-signal stability region, system identification technique, wind power generation.**

I. INTRODUCTION

WIND power generation has experienced rapid growth in recent years as a form of environmentally friendly power. The globally installed capacity of wind power reached a remarkable 840.9 GW by 2022, accounting for an increase of 8.6% over the previous year [1]. Notably, permanent magnet synchronous generator (PMSG), recognized for their cost-effectiveness and high efficiency, have gradually become one of the dominant types in wind power generations [2]. With the continuous increase in wind power generations, wind farms with PMSGs significantly impact grid stability and reliability, resulting in small-signal stability issues. For instance, several oscillation incidents have occurred in areas, such as North China, the ECROT region, and Texas, leading to damage to power generation equipment and disconnections of wind farms from the power systems [3].

Small-signal stability analysis of power electronic devices in renewable energy systems generally employs state–space and impedance methods [4]. The state–space method requires the state–space matrix of the entire system and relies on known system parameters and structures. On the other hand, it only requires modification of the impedance of the corresponding changed parts when system changes occur. In addition, impedance can be obtained through frequency scan, which is independent of known parameters [5]. Therefore, the impedance analysis is commonly employed to explore the small-signal stability of wind farms.

The detailed impedance of large-scale wind power plant (WPP) encounters “curse of dimensionality” in numerical calculation. To reduce the order of the impedance and increase the efficiency of the stability analysis, an equivalent impedance for WPPs could be utilized [6]. The capacity-weighted averaging and parameter identification methods are commonly used to obtain the equivalent impedance. The capacity-weighted averaging method aggregates the physical parameters of wind turbine generators (WTGs) to attain parameters of the equivalent wind turbine [7]. The parameter identification method estimates the parameters of the equivalent WTG based on either physical measurements or simulation data [8]. However, these equivalent methods are predominantly derived for large signal analysis. The objective of equivalence is often to ensure consistency of time-domain waveforms [9]. The accuracy of the impedance characteristics in the frequency domain is difficult to be guaranteed. Therefore, the equivalent methods for large-signal analysis are not applicable to the small-signal stability analysis [10], [11].

To improve the accuracy of the aggregated impedance, there has been literature comparing the frequency domain indexes, such as the dominant mode and synchronous oscillation frequency [12], [13]. Such methods focus on the equivalence in a specific frequency band, and the equivalent model cannot reflect the dynamic characteristics of the entire frequency band. The frequency band is divided into low frequency, medium frequency, and high frequency with an objective of impedance

---

Manuscript received 6 September 2023; revised 8 January 2024; accepted 12 March 2024. Date of publication 29 April 2024; date of current version 20 June 2024. Recommended for publication by Associate Editor K. Gunawardane. *(Corresponding author: Shiyao Qin.)*

Shiyao Qin and Shaolin Li are with the National Key Laboratory of Renewable Energy Grid-Integration (China Electric Power Research Institute), Beijing 100192, China (e-mail: qinshy@epri.sgcc.com.cn; lishaolin@epri.sgcc.com.cn).

Peng Wang, Haoran Zhao, Jinlong Wang, and Jia Luo are with the School of Electrical Engineering, Shandong University, Jinan 250061, China (e-mail: p.wang@sdu.edu.cn; hzhao@sdu.edu.cn; 202220673@mail.sdu.edu.cn; jialuo@mail.sdu.edu.cn).

Color versions of one or more figures in this article are available at https://doi.org/10.1109/TPEL.2024.3392265.

Digital Object Identifier 10.1109/TPEL.2024.3392265

consistency of wind farm [14]. Such frequency band division is generally rough, resulting in deviations under time-varying operating points. Moreover, the single-machine equivalence is used, which is difficult to reflect the interactive dynamics in WPP. An efficient and accurate method for impedance aggregation is still missing for small-signal stability analysis under varying operating points.

Taking into consideration the time-varying wind speed and power commands, stability analysis under varying operating points should be addressed. The stability region of wind farms is valuable for stability assessment under varying operating points. The stability region boundary of a single parameter could be obtained from the point-by-point method. In Hu et al.'s [15] work, the stability region of the series compensation value is obtained from point-by-point analysis. However, point-by-point methods suffer from a significant computational burden, making it difficult to apply online, especially for determining a multiparameter stability region. To construct the multiparameter stability region online, the point-by-point method can be transformed into a classification problem of whether the system is stable or unstable at given parameters, thereby significantly reducing the computational load. Support vector machine (SVM) is adaptive to complex and high-dimensional data classification. SVMs have been applied in areas, such as motor state analysis and fault prediction [16], [17], [18]. The stability region is trained offline with high accuracy. For online applications, the stability performed at given operating points can be predicted efficiently. However, in practical WPPs, the model training should be performed online to estimate the multiparameter stability region boundary since the boundary changes with the grid impedance. Moreover, a multiparameter stability region boundary is required since the power, wind speed, and other operating points change in practical applications. To estimate the multiparameter boundary, SVMs need to involve a bulk of samples in the training process to find the optimal classification hyperplane. This leads to a computational burden, resulting in difficulty in online training.

This article proposes a stability region estimation based on the aggregated impedance of the WPP. First, a mechanism-data-driven aggregation method is proposed to establish equivalent impedance of multiple WTGs. This resolves the problem of the computational complexity of the detailed impedance model of the WPP. Second, a fuzzy support vector machine (FSVM) is used to construct the multiparameter stability boundary of the WPP. The importance of different samples of the stability index is distinguished by the weighted Mahalanobis distance, significantly reducing the computational burden of online construction of the stability region. Finally, the stability performance is proven to be enhanced by adjusting the operating point of the WTG and the static var generator (SVG). The stability region estimation and enhancement are verified by numerical simulations in MATLAB/Simulink and experiments in the controller-hardware-in-loop platform.

The rest of this article is organized as follows. Section II establishes the detailed impedance of the WPP with PMSGs. In Section III, a mechanism-data driven aggregation method is proposed to derive the equivalent impedance of multiple WTGs. Section IV develops the stability boundary using the FSVM. Case studies are given in Section V. Finally, Section VI concludes this article.

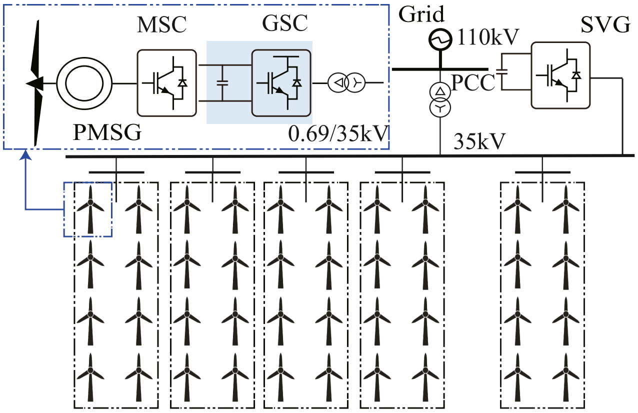

Fig. 1. WPP with PMSGs.

II. Detailed Impedance of Direct-Drive Wind Turbines and WPP

The topology of a typical WPP is depicted in Fig. 1. The WPP comprises multiple branches, each with several WTGs. The WPP is connected to the ac grid through a stepup transformer. A SVG is connected to the point of common coupling (PCC) of the WPP to compensate for reactive power.

A. *Detailed Impedance Model of PMSG*

The structure of a PMSG is depicted in the top-left corner of Fig. 1. The PMSG is connected to the WPP via back-to-back converters and a stepup transformer. The machine-side converter (MSC) employs rotor flux-oriented control to regulate the electromagnetic torque, thus tracking the active power command. The grid-side converter (GSC) uses grid voltage-oriented control to maintain constant dc voltage, thereby realizing dc voltage stability. The presence of the dc bus decouples the dynamics of the machine side and the grid side. Therefore, the dynamics of the machine and the machine-side converter can be ignored in the impedance analysis of PMSG, and the impedance of the GSC dominates the frequency domain analysis [19]. As such, the overall impedance can be expressed as [20]

$$\boldsymbol{Z}_{\mathrm{WTG}}(s) = \frac{\boldsymbol{Z}_{\mathrm{g}}(s) + \boldsymbol{Z}_{\mathrm{gsc}}(s) + \boldsymbol{Z}_{\mathrm{ui}}(\boldsymbol{Z}_{\mathrm{cu}} - \boldsymbol{Z}_{\mathrm{ci}}\boldsymbol{Z}_{\mathrm{g}})}{\boldsymbol{E} - \boldsymbol{Z}_{\mathrm{gsc}}(s)\boldsymbol{Z}_{\mathrm{ig}}(s) + \boldsymbol{Z}_{\mathrm{ug}}(s) - \boldsymbol{Z}_{\mathrm{ui}}\boldsymbol{Z}_{\mathrm{ci}}} \quad (1)$$

where s is the Laplace operator, $\boldsymbol{E}$ is the unit matrix, $\boldsymbol{Z}_{\mathrm{g}}$ is the filter impedance matrix, $\boldsymbol{Z}_{\mathrm{gsc}}$ is related to the inner current controller, $\boldsymbol{Z}_{\mathrm{ig}}$ is related to the current transformation, $\boldsymbol{Z}_{\mathrm{ug}}$ is related to the voltage transformation, $\boldsymbol{Z}_{\mathrm{ui}}$ is related to the outer voltage and inner current controllers, $\boldsymbol{Z}_{\mathrm{cu}}$ and $\boldsymbol{Z}_{\mathrm{ci}}$ are related to the dc dynamics. The formulations of those matrices are given in Appendix. The SVG primarily comprises a converter and a capacitor at the dc link, as shown in the top-right corner of Fig. 1. The impedance of SVG is similar to that of the PMSG, which takes into account only the GSC. However, the SVG provides only reactive power. The impedance model of the SVG can be expressed as follows:

$$\boldsymbol{Z}_{\mathrm{SVG}}(s)=\begin{bmatrix} Z_{\mathrm{dd}}^{\mathrm{SVG}}(s) & Z_{\mathrm{dq}}^{\mathrm{SVG}}(s) \\ Z_{\mathrm{qd}}^{\mathrm{SVG}}(s) & Z_{\mathrm{qq}}^{\mathrm{SVG}}(s)\end{bmatrix}. \tag{2}$$

B. Impedance Aggregation of WPP

The impedance of the individual devices in a WPP is established based on their respective dq coordinate systems oriented by the device terminal voltages. Due to the existence of collection lines, the voltages at each device terminal are different. As such, the dq coordinate systems of the individual device are not the same. Therefore, a unified dq coordinate system is defined for the WPP and transforms the impedance of each component into the unified dq coordinate system. Then, a lumped impedance of the WPP is established.

The PCC is selected as the reference node for the WPP in Fig. 1. The steady-state operating point of each node and the angle difference θ_{WTG} between each node and the reference node can be obtained through power flow calculation. In the unified dq coordinate system, the WTG impedance can be expressed as

$$\boldsymbol{Z}_{\mathrm{WTG}}^{\mathrm{u}}(s)=\boldsymbol{T}_{\mathrm{dq}}\boldsymbol{Z}_{\mathrm{WTG}}(s)\boldsymbol{T}_{\mathrm{dq}}^{-1} \tag{3}$$

where $\boldsymbol{T}_{\mathrm{dq}}$ is defined as

$$\boldsymbol{T}_{\mathrm{dq}}=\begin{bmatrix} \cos(\theta_{\mathrm{WTG}}) & \sin(\theta_{\mathrm{WTG}}) \\ -\sin(\theta_{\mathrm{WTG}}) & \cos(\theta_{\mathrm{WTG}})\end{bmatrix}. \tag{4}$$

The impedance of all devices in the WPP, such as $\boldsymbol{Z}_{\mathrm{WTG}}^{\mathrm{u}}(s)$ and $\boldsymbol{Z}_{\mathrm{SVG}}(s)$, are 2-D matrices. In the unified dq coordinate system, the impedance satisfies the circuit rule of series and parallel connections. Focusing on a branch of the WPP, the impedance $\boldsymbol{Z}_{\mathrm{br}}(s)$ of each branch in the WPP can be aggregated

$$\boldsymbol{Z}_{\mathrm{br}}(s)=\begin{bmatrix} Z_{\mathrm{br,dd}}(s) & Z_{\mathrm{br,dq}}(s) \\ Z_{\mathrm{br,qd}}(s) & Z_{\mathrm{br,qq}}(s)\end{bmatrix}. \tag{5}$$

The detailed impedance of the WPP, denoted as $\boldsymbol{Z}_{\mathrm{farm}}(s)$, can be obtained from the parallel circuit calculation

$$\boldsymbol{Z}_{\mathrm{farm}}(s)=\boldsymbol{Z}_{\mathrm{br1}}(s)\parallel\boldsymbol{Z}_{\mathrm{br2}}(s)\parallel\cdots\parallel\boldsymbol{Z}_{\mathrm{SVG}}(s). \tag{6}$$

III. MECHANISM-DATA DRIVEN IMPEDANCE AGGREGATION AND PARAMETER IDENTIFICATION

A WPP consisting of homogenous WTGs can be represented by a single scaled unit for the time-domain large-signal modeling [21]. However, the impedance in the frequency domain exhibits strong coupling characteristics across wide-band frequency, making it difficult to ensure accuracy with a single equivalent unit. Multimachine equivalent modeling for impedance calculation is preferred, resulting in balanced accuracy and computational efficiency. First, approximately aggregated impedance of the WTG, the transformer, and the collection lines are developed. Subsequently, key parameters influencing impedance aggregation are identified and recalculated with the data-driven method to improve the accuracy of the approximate aggregated impedance. The proposed mechanism-data-driven method of the equivalent impedance can be extended to other VSC-dominated systems, such as photovoltaic and energy storage systems.

A. Approximate Calculation of Impedance Aggregation for WTGs

For the convenience of WTG impedance aggregation, it is assumed that the N turbines of a WPP branch are directly connected in parallel. Without the influence of the collector line and transformer impedance, the branch impedance can be described by a parallel connection of the impedance of multiple WTGs. Such a structure facilitates the derivation of the aggregated impedance model of the WTGs. Such an assumption is reasonable since the WTG impedance plays a dominant role in WPP impedance [22]. Besides, the electrical parameters of WTGs within a branch are usually identical, and so are the control parameters. The impedance of the WTGs is distinguished by their operating point, such as the active and reactive power.

For the convenience of impedance aggregation, the dynamic of the dc voltage regulation is neglected first in the mechanism-driven approximation. The corresponding control parameters of the dc voltage could be later modified by data-driven approach. As such, the terms related to the outer voltage controls $\boldsymbol{Z}_{\mathrm{ui}}$ are neglected. The admittance $\boldsymbol{Y}_{\mathrm{WTG},n}(s)$ of the nth WTG is then given by

$$\boldsymbol{Y}_{\mathrm{WTG},n}(s)=\frac{\boldsymbol{E}-\boldsymbol{Z}_{\mathrm{gsc}}(s)\boldsymbol{Z}_{\mathrm{ig},n}(s)+\boldsymbol{Z}_{\mathrm{ug},n}(s)}{\boldsymbol{Z}_{\mathrm{g}}(s)+\boldsymbol{Z}_{\mathrm{gsc}}(s)} \tag{7}$$

where $\boldsymbol{Z}_{\mathrm{ig}}$ is related to the current transformation, and $\boldsymbol{Z}_{\mathrm{ug}}$ is related to the voltage transformation. Both matrices are dependent on the operating point.

Considering N WTGs of a branch in parallel, the aggregated impedance $\boldsymbol{Y}_{\mathrm{br,WTGs}}^{\mathrm{cal}}$ of a branch is given by

$$\boldsymbol{Y}_{\mathrm{br,WTGs}}^{\mathrm{cal}}=\boldsymbol{Y}_{\mathrm{WTG},1}+\cdots+\boldsymbol{Y}_{\mathrm{WTG},n}+\cdots+\boldsymbol{Y}_{\mathrm{WTG},N}. \tag{8}$$

Inserting (7) to (8) gives

$$\boldsymbol{Y}_{\mathrm{br,WTGs}}^{\mathrm{cal}}=\frac{\boldsymbol{E}-\frac{\boldsymbol{Z}_{\mathrm{gsc}}}{N}\cdot\sum_{n=1}^{N}\boldsymbol{Z}_{\mathrm{ig},n}+\frac{\sum_{n=1}^{N}\boldsymbol{Z}_{\mathrm{ug},n}}{N}}{\frac{\boldsymbol{Z}_{\mathrm{g}}}{N}+\frac{\boldsymbol{Z}_{\mathrm{gsc}}}{N}} \tag{9}$$

where the superscript “cal” denotes the calculated parameter values, and the matrices $\boldsymbol{Z}_{\mathrm{g}}$, $\boldsymbol{Z}_{\mathrm{gsc}}$, $\boldsymbol{Z}_{\mathrm{ig,n}}$, and $\boldsymbol{Z}_{\mathrm{ug,n}}$ are given by (41)–(45) in the appendix.

Referring to (9) and (44), the aggregated term for the Park transformation of current is formulated as

$$\sum_{n=1}^{N}\boldsymbol{Z}_{\mathrm{ig},n}=\begin{bmatrix} 0 & Z_{\mathrm{PLL}}\cdot\sum_{n=1}^{N}i_{\mathrm{gq},n} \\ 0 & -Z_{\mathrm{PLL}}\sum_{n=1}^{N}i_{\mathrm{gd},n}\end{bmatrix} \tag{10}$$

where Z_{PLL} is the same as that of a single WTG; $i_{\mathrm{gd},n}$ and $i_{\mathrm{gq},n}$ are the ac current in Fig. 2. The aggregation principle for the PLL is then given by

$$k_{\mathrm{p,pll}}^{\mathrm{cal}}=k_{\mathrm{p,pll}},\quad k_{\mathrm{i,pll}}^{\mathrm{cal}}=k_{\mathrm{i,pll}}. \tag{11}$$

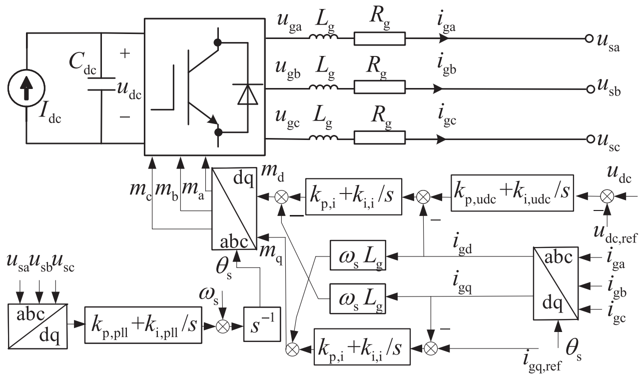

Fig. 2. Typical circuit and control structure of the GSC.

Referring to (9) and (45), the aggregated term for the Park transformation of voltage is formulated as

$$\frac{1}{N}\sum_{n=1}^{N}\boldsymbol{Z}_{\mathrm{ug},n}=\begin{bmatrix}0 & Z_{\mathrm{PLL}}\cdot\sum_{n=1}^{N}u_{\mathrm{gq},n}/N\\ 0 & -Z_{\mathrm{PLL}}\sum_{n=1}^{N}u_{\mathrm{gd},n}/N\end{bmatrix}\tag{12}$$

where $v_{\mathrm{gd},n}$ and $v_{\mathrm{gq},n}$ are the ac terminal voltage of the converter in Fig. 2 According to $\boldsymbol{Z}_{\mathrm{gsc}}/N$ in (9) and (42), the aggregated current controller can be established as

$$k_{\mathrm{p,i}}^{\mathrm{cal}}=k_{\mathrm{p,i}}/N,\quad k_{\mathrm{i,i}}^{\mathrm{cal}}=k_{\mathrm{i,i}}/N\tag{13}$$

where k_{p} and k_{i} represent the proportional and integral coefficients, respectively. According to $\boldsymbol{Z}_{\mathrm{g}}/N$ in (9) and (41), approximated calculation for the filter impedance is given by

$$L_{\mathrm{g}}^{\mathrm{cal}}=L_{\mathrm{g}}/N,\quad R_{\mathrm{g}}^{\mathrm{cal}}=R_{\mathrm{g}}/N.\tag{14}$$

Other filters, such as the LCL filter, could also be applied besides the employed L filters. The proposed parallel-calculation method is applicable to LCL filters. To ensure ease of analysis and illustration, approximate calculation of impedance aggregation is performed only for WTGs equipped with L filters.

B. Approximate Calculation of Aggregated Impedance for Collection Lines and Transformers

The stepup transformers of the WTGs in a branch are equivalently treated as a scaled-up transformer located at the terminal of the equivalent WTG. The capacity of this scaled-up transformer is the sum of the capacities of all WTG transformers in a branch. The impedance of the scaled-up transformer is described by a parallel combination of the impedance of WTG transformers. Hence, the formulation for the impedance $\boldsymbol{Z}_{\mathrm{br,T}}^{\mathrm{cal}}$ of the scaled-up transformer is given follows:

$$\boldsymbol{Z}_{\mathrm{br,T}}^{\mathrm{cal}}=\boldsymbol{Z}_{\mathrm{T}}/N\tag{15}$$

where $\boldsymbol{Z}_{\mathrm{T}}$ is the transformer impedance of a single WTG.

The collection line is approximated using a constant power loss method. It is assumed that the power loss on the collection line remains the same before and after the equivalent transformation. The equivalent impedance of the collection network for the branch is then given as follows:

$$\boldsymbol{Z}_{\mathrm{br,L}}^{\mathrm{cal}}=\sum_{i=1}^{N}\left(P_{\mathrm{L},i}^{2}\boldsymbol{Z}_{\mathrm{L},i}\right)/\left(\sum_{i=1}^{N}P_{\mathrm{L},i}\right)^{2}\tag{16}$$

where $\boldsymbol{Z}_{\mathrm{L},i}$ denotes the line impedance for the ith WTG, and $P_{\mathrm{L,i}}$ represents the power loss of the impedance $\boldsymbol{Z}_{\mathrm{L},i}$.

With knowledge of the aggregated impedance, the aggregated impedance $\boldsymbol{Z}_{\mathrm{br}}^{\mathrm{cal}}$ of a branch based on the mechanism-driven method is given by

$$\boldsymbol{Z}_{\mathrm{br}}^{\mathrm{cal}}=\left(\boldsymbol{Y}_{\mathrm{br,WTGs}}^{\mathrm{cal}}\right)^{-1}+\boldsymbol{Z}_{\mathrm{br,T}}^{\mathrm{cal}}+\boldsymbol{Z}_{\mathrm{br,L}}^{\mathrm{cal}}\tag{17}$$

where the subscripts WTGs, T, and L denote the WTGs, the transformer, and the line, respectively.

C. Identification and Calculation of Key Parameters for Improving Accuracy of Aggregated Impedance

The aggregated impedance in (17) obtained from mechanism-driven approximation must have errors since the interaction of the WTG and the lines in approximate calculation of impedance aggregation are neglected. The accuracy of the mechanism-driven aggregated impedance can be improved by adjusting multiple key parameters. Traditional methods for key parameter identification are often targeted at the time-domain equivalent model under large disturbances. When applied to small-signal model equivalence, it is difficult to ensure the accuracy of the equivalent impedance in the wide frequency range. Since the impedance shows strong nonlinearity across a wide frequency band, this section proposes a method for key parameter identification and modification across different frequency bands.

1) Sensitivity Analysis of Impedance Parameter Across Wide Frequency Band: Since the impedance of a WTG is usually much larger than the combined impedance of the collection lines and transformers, the parameters of the WTG are chosen as the target parameter for identification. The mechanism-driven aggregated impedance $\boldsymbol{Y}_{\mathrm{br,WTGs}}^{\mathrm{cal}}$ in (9) obtained from parallel circuit analysis is a function of circuit parameters and control parameters. The set $\boldsymbol{x}_{\mathrm{WTG}}^{\mathrm{para}}$ of circuit and control parameters, potentially to be identified, is defined as follows:

$$\boldsymbol{x}_{\mathrm{WTG}}^{\mathrm{para}}=\left\{k_{\mathrm{p,udc}}^{\mathrm{cal}},k_{\mathrm{i,udc}}^{\mathrm{cal}},k_{\mathrm{p,i}}^{\mathrm{cal}},k_{\mathrm{i,i}}^{\mathrm{cal}},k_{\mathrm{p,pll}}^{\mathrm{cal}},k_{\mathrm{i,pll}}^{\mathrm{cal}},R_{\mathrm{g}}^{\mathrm{cal}},L_{\mathrm{g}}^{\mathrm{cal}}\right\}\tag{18}$$

where $k_{\mathrm{p,udc}}^{\mathrm{cal}}, k_{\mathrm{i,udc}}^{\mathrm{cal}}$ are the calculated parameters of the dc voltage regulation. The dc voltage of the aggregated WTG is similar to that of the original ones. Therefore, the calculated parameters can be set to the same as that of the original WTG.

To obtain the key parameters affecting the impedance characteristics, an impedance sensitivity analysis is performed. The sensitivity $\boldsymbol{K}_{\mathrm{s}}$ of the impedance $\boldsymbol{Z}_{\mathrm{br}}^{\mathrm{cal}}(s)$ to the parameters $\boldsymbol{x}_{\mathrm{WTG}}^{\mathrm{para}}$ can be expressed as follows:

$$\boldsymbol{K}_{\mathrm{s}}(x_i,s)=\partial\boldsymbol{Z}_{\mathrm{br}}^{\mathrm{cal}}(s)/\partial x_i,\quad x_i\in\boldsymbol{x}_{\mathrm{WTG}}^{\mathrm{para}}.\tag{19}$$

2) Identification of Key Parameters and Division of Frequency Band: The sensitivity $\boldsymbol{K}_{\mathrm{s}}(s)$ in (19) is a function of the Laplace operator s. The sensitivity exhibits nonlinear characteristics over a wide frequency range. The sensitivity $\boldsymbol{K}_{\mathrm{s}}(x_i,s)$ is calculated at a step of 1 Hz within the wide frequency range of

0–1000 Hz. At each frequency s_j, the k variables with the highest sensitivity are identified, denoted as $\boldsymbol{x}_{\mathrm{id},l}$. The wide frequency band is divided into l regions according to the variations of the k dominant factors. The lth region ranges from $s_{l,\min}$ to $s_{l,\max}$. In the lth region, the parameter $\boldsymbol{x}_{\mathrm{id},l}$ to be identified are defined as follows:

$$\begin{cases} \boldsymbol{x}_{\mathrm{id},l} = \{x_i | i = 1, \ldots, k; x_i \in \boldsymbol{x}_{\mathrm{WTG}}^{\mathrm{para}}\} \\ \quad \text{s.t. } s_{l,\min} < s < s_{l,\max} \end{cases} \tag{20}$$

where l denotes the lth region of the frequency band, and there are k parameters to be identified in each frequency band. Based on the accuracy and speed of identification, the parameter k can be optimized.

3) Correction of Key Parameters Affecting Equivalent Impedance Based on Data-Driven Method: The deviation between the mechanism-driven aggravated impedance and the detailed impedance is corrected by identifying the key parameters of the equivalent impedance in each frequency band. The key parameters in (20) in each frequency band are identified with the data-driven method. The particle swarm optimization (PSO) algorithm is utilized for the segmented identification of key parameters affecting the aggregated impedance. The PSO algorithm is a kind of adaptive iterative algorithm based on global population search, which has the advantage of fast convergence speed. For parameter identification in the lth region of the frequency band, the fitness function can be written as follows:

$$\boldsymbol{x}_{\mathrm{id},l}^{\mathrm{eq}} = \begin{cases} \arg \min\limits_{\boldsymbol{x}_{\mathrm{id},l}} \sum \left| \boldsymbol{Z}_{\mathrm{br}}(s) - \boldsymbol{Z}_{\mathrm{br}}^{\mathrm{cal}}(s, \boldsymbol{x}_{\mathrm{id},l}) \right| \\ \quad \text{s.t. } s_{l,\min} < s < s_{l,\max} \end{cases} \tag{21}$$

where $\boldsymbol{Z}_{\mathrm{br}}$ represents the original impedance of the branch, $\boldsymbol{Z}_{\mathrm{br}}^{\mathrm{cal}}$ represents the mechanism-driven aggregated impedance of a branch, s is the Laplace operator in the frequency domain, and $s_{l,\min}, s_{l,\max}$ represent the boundary points of the lth region of frequency band. The key parameters $\boldsymbol{x}_{\mathrm{id},l}$ affecting impedance in the lth region of the frequency band is given by (20). By precisely modifying the key parameters, the deviations in the mechanism-driven aggregated impedance $\boldsymbol{Z}_{\mathrm{br}}^{\mathrm{cal}}$ are corrected. This significantly enhances the accuracy of the equivalent impedance.

According to the mechanism-driven aggregated impedance in $\boldsymbol{Z}_{\mathrm{br}}^{\mathrm{cal}}$ (17) and the data-driven modified key parameters $\boldsymbol{x}_{\mathrm{id},l}^{\mathrm{eq}}$ in (21), the mechanism-data driven aggregated impedance is formulated as

$$\boldsymbol{Z}_{\mathrm{br}}^{\mathrm{eq}}(s) = \boldsymbol{Z}_{\mathrm{br}}^{\mathrm{cal}}\left(s, \boldsymbol{x}_{\mathrm{id},l}^{\mathrm{eq}}\right), s_{l,\min} < s < s_{l,\max}. \tag{22}$$

For the WPP shown in Fig. 1, it is assumed that there are M branches and one SVG. The equivalent impedance of the mth branch can be expressed as $\boldsymbol{Z}_{\mathrm{br},m}^{\mathrm{eq}}$. With knowledge of the branch equivalent impedance in (22) and the SVG impedance $\boldsymbol{Z}_{\mathrm{SVG}}$ in (2), the WPP impedance can be obtained from parallel circuit calculation

$$\left(\boldsymbol{Z}_{\mathrm{farm}}^{\mathrm{eq}}\right)^{-1} = \left(\boldsymbol{Z}_{\mathrm{br},1}^{\mathrm{eq}}\right)^{-1} + \cdots + \left(\boldsymbol{Z}_{\mathrm{br},M}^{\mathrm{eq}}\right)^{-1} + \boldsymbol{Z}_{\mathrm{SVG}}^{-1}. \tag{23}$$

IV. ONLINE ESTIMATION OF STABILITY REGION BASED ON FSVM

This section focuses on the online estimation of the stability region. The safety margin index at diverse operating points is established according to the equivalent impedance developed in Section III. Subsequently, the FSVM is used to establish the stability region boundary. The proposed method can accurately and efficiently quantify the boundary of the small-signal stability region in a high-dimensional parameter space.

A. Definition of Stability Region for WPP

The impedance of a WPP is dependent on the system operating point, the circuit parameters, and the control parameters. Among these parameters, the operating point is changeable in practical applications. The stability region of the active power of the WTGs and the reactive power of the SVG is considered. The active power of a branch and the reactive power of SVG are selected as state variables, which define the parameter space

$$\boldsymbol{x}_{\mathrm{farm}} = \{P_{\mathrm{br}1}, \ldots, P_{\mathrm{br}M}, \boldsymbol{Q}_{\mathrm{SVG}}\}, \boldsymbol{x}_{\mathrm{farm},h} \subset \mathbb{R}^{M+1} \tag{24}$$

where M represents the number of branches in the WPP, and $\mathbb{R}$ denotes the real number space.

According to (23), the impedance of the WPP under a given operating point $\boldsymbol{x}_{\mathrm{farm}}$ is represented as $\boldsymbol{Z}_{\mathrm{farm}}^{\mathrm{eq}}(\boldsymbol{x}_{\mathrm{farm}}, s)$. Combined with the grid impedance $\boldsymbol{Z}_{\mathrm{grid}}(s)$, the lumped impedance $\boldsymbol{Z}_{\mathrm{lump}}(\boldsymbol{x}_{\mathrm{farm}}, s)$ of the grid-tied WPP can be calculated as

$$\boldsymbol{Z}_{\mathrm{lump}}(\boldsymbol{x}_{\mathrm{farm}}, s) = \boldsymbol{Z}_{\mathrm{farm}}^{\mathrm{eq}}(\boldsymbol{x}_{\mathrm{farm}}, s) + \boldsymbol{Z}_{\mathrm{grid}}(s). \tag{25}$$

The stability performance at a specific operating condition can be determined by calculating the determinant zeros σ_i of the lumped impedance $\boldsymbol{Z}_{\mathrm{lump}}(\boldsymbol{x}_{\mathrm{farm}}, s)$, that is $|\boldsymbol{Z}_{\mathrm{lump}}(\boldsymbol{x}_{\mathrm{farm}}, \sigma_i)| = 0$. The determinant zeros of the lumped impedance correspond to the system eigenvalues [23]. Therefore, the system is stable if and only if the real part of all zeros of the lumped impedance determinant is less than zero. Otherwise, the system is unstable. Moreover, the smaller the maximum real part of the determinant zeros of the lumped impedance, the larger the stability margin of the system. Therefore, the stability margin index $M_{\mathrm{G}}(\boldsymbol{x}_{\mathrm{farm}})$ at the operating point $\boldsymbol{x}_{\mathrm{farm}}$ is defined as

$$M_{\mathrm{G}}(\boldsymbol{x}_{\mathrm{farm}}) = \max\left\{\mathrm{Re}(\sigma_i) \,|\, |\boldsymbol{Z}_{\mathrm{lump}}(\boldsymbol{x}_{\mathrm{farm}}, \sigma_i)| = 0\right\} \tag{26}$$

where σ_i is the determinant zero of the lumped impedance. The system is stable when $M_{\mathrm{G}}(\boldsymbol{x}_{\mathrm{farm}}) > 0$. When $M_{\mathrm{G}}(\boldsymbol{x}_{\mathrm{farm}}) < 0$, the system is unstable. According to (26), the stability region can be represented as a set of operating conditions that make the system stability index greater than zero. The stability region in the parameter space $\boldsymbol{x}_{\mathrm{farm}}$ in (24) is defined as

$$\Omega_{\mathrm{farm}} = \left\{\boldsymbol{x}_{\mathrm{farm}} \subset \mathbb{R}^{M+1} \,|\, M_{\mathrm{G}}(\boldsymbol{x}_{\mathrm{farm}}) > 0\right\}. \tag{27}$$

B. Construction of the Stability Index Dataset

A stability index dataset is required for the construction of stability region using machine-learning methods. First, the variation range of the state variable $\boldsymbol{x}_{\mathrm{farm}}$ in (24) is determined. This range is typically constrained by factors, such as the wind turbine mechanical power, converter capacity, and static stability limit. Subsequently, within the range of these operational parameters, H samples of $\boldsymbol{x}_{\text{farm}}$ are randomly selected, denoted as $\{\boldsymbol{x}_{\text{farm},h} | h = 1, 2, \ldots, H\}$. Second, at a given operating state $\boldsymbol{x}_{\text{farm},h}$, the equivalent impedance $\boldsymbol{Z}_{\text{br}}^{\text{eq}}$ in (22) of each branch is obtained as (22). Third, the equivalent impedance of the WPP is developed from the branch impedance and SVG impedance, as given by $\boldsymbol{Z}_{\text{farm}}^{\text{eq}}$ in (23). Finally, the corresponding stability index $M_{\text{G},h}(\boldsymbol{x}_{\text{farm},h})$ is calculated by (26), thereby constructing the stability index dataset

$$\boldsymbol{M}_{\text{farm}} = \{\boldsymbol{x}_{\text{farm},h}, M_{\text{G},h} | h = 1, 2, \ldots, H\} \tag{28}$$

where the subscript h represents the hth sample, and the subscript H denotes the total number of samples.

C. FSVM for Stability Boundary Identification

Based on the stability index dataset $\boldsymbol{M}_{\text{farm}}$ in (28), machine learning algorithms enable the identification of the stability boundary. Online identification is needed since the boundary changes with parameters such as the grid impedance and the pitch angle of the wind turbines. As a supervised machine learning, the SVM is employed. The SVM encounters slow training speeds for large-scale data, resulting in obstacles to timely boundary provision. For this reason, an FSVM algorithm is employed [24]. The FSVM assigns a fuzzy membership degree to each sample to differentiate the sample importance, resulting in an optimal classification surface and reducing the impacts of noise samples. This enhances computational efficiency while improving classification accuracy.

The stability data $\boldsymbol{M}_{\text{farm}}$ in (28) are labeled according to the selected boundary index $M_{\text{G}} = \varepsilon$. For the hth sample $\{\boldsymbol{x}_{\text{farm},h}, M_{\text{G},h}\}$, it is labeled as positive sample when $M_{\text{G},h} > \varepsilon$. The positive sample is defined as $y_h = 1$. When $M_{\text{G},h} < \varepsilon$, the sample is labeled as the negative sample, that is $y_h = -1$. The importance of the sample is assessed by fuzzy membership, which is defined as $s_h \in (0, 1]$. The fuzzy membership s_h indicates the degree to which the sample $\boldsymbol{x}_{\text{farm},h}$ belongs to the positive or negative class. Determining the stability region boundary is generalized as a classification problem. Considering different values of $M_{\text{G}} = \varepsilon$, multiple boundaries of relative stability can be obtained, forming a gradient stability region.

Due to the complex mapping between the labeled stability indexes y_h and the operating point $\boldsymbol{x}_{\text{farm}}$, it is difficult to linearly classify the original samples in the original parameter space $\mathbb{R}$. By using the mapping function $\phi(\boldsymbol{x}_{\text{farm}})$, the original parameter space $\mathbb{R}$ can be mapped to a higher dimensional Hilbert space $\mathbb{H}$

$$\phi(\boldsymbol{x}_{\text{farm}}) = (\phi_1(\boldsymbol{x}_{\text{farm}}), \phi_2(\boldsymbol{x}_{\text{farm}}), \ldots, \phi_c(\boldsymbol{x}_{\text{farm}}))^{\text{T}} \tag{29}$$

where the subscript c represents the dimension of the high-dimensional Hilbert space $\mathbb{H}$.

The decision boundary hyperplane in the high-dimensional Hilbert space $\mathbb{H}$ is developed by replacing $\boldsymbol{x}_{\text{farm}}$ with the feature vector $\phi(\boldsymbol{x}_{\text{farm}})$

$$\boldsymbol{\omega}^{\text{T}}\phi(\boldsymbol{x}_{\text{farm}}) + \boldsymbol{b} = 0 \tag{30}$$

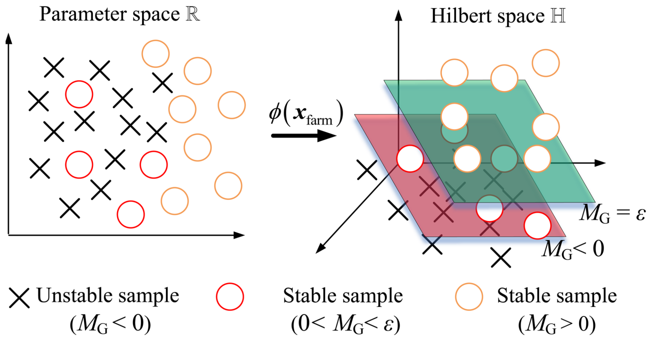

Fig. 3. Illustration of classification in high-dimensional Hilbert space.

where $\boldsymbol{\omega}$ is the coefficient vector, and $\boldsymbol{b}$ is the offset term. An illustration of the decision boundary hyperplane is shown in Fig. 3. Multiple decision boundaries can be established by selecting different criteria $M_{\text{G}} = \varepsilon$.

To obtain the optimal hyperplane for the classification of the samples, the following optimization problem needs to be solved:

$$\min_{\boldsymbol{\omega},b,\xi} \frac{1}{2}\|\boldsymbol{\omega}\|^2 + C\sum_{h=1}^{H} s_h\xi_h$$
$$\text{s.t. } y_h\left(\boldsymbol{\omega}^{\text{T}}\phi\left(\boldsymbol{x}_{\text{farm},h}\right)+b\right) \geq 1-\xi_h (h = 1, 2, \ldots, H) \tag{31}$$

where C is the penalty factor, s_h is the fuzzy membership, and ξ_h is the slack factor. The term $s_h\xi_h$ essentially assigns different weights to the classification errors. The smaller this product, the greater the likelihood of being classified correctly. A smaller s_h corresponds to a smaller role of the slack factor in the optimization process.

The term $\|\boldsymbol{\omega}\|^2$ introduces the inner product of the samples after high-dimensional mapping. It is complex and time-consuming to calculate the inner product in the high-dimensional space $\mathbb{H}$. To address this issue, the kernel function $k(\boldsymbol{x}_{\text{farm},h}, \boldsymbol{x}_{\text{farm},j})$ is employed. This allows to calculate the inner product in the original feature space $\mathbb{X}$

$$k\left(\boldsymbol{x}_{\text{farm},h}, \boldsymbol{x}_{\text{farm},j}\right) = \phi\left(\boldsymbol{x}_{\text{farm},h}\right)^{\text{T}}\phi\left(\boldsymbol{x}_{\text{farm},j}\right). \tag{32}$$

The dual form of the original optimization problem using the kernel function is given as follows:

$$\max_{\alpha} \sum_{h=1}^{H}\alpha_h - \frac{1}{2}\sum_{h=1}^{H}\sum_{j=1}^{H}\alpha_h\alpha_j y_h y_j k\left(\boldsymbol{x}_{\text{farm},h}, \boldsymbol{x}_{\text{farm},j}\right)$$
$$\text{s.t. } \sum_{h=1}^{H}\alpha_h y_h = 0, 0 \leq \alpha_h \leq s_h C, \quad h = 1, 2, \ldots, H. \tag{33}$$

By solving the dual problem, the stability region boundary in its original dimension can be obtained as

$$\sum_{h=1}^{H}\alpha_h y_h k\left(\boldsymbol{x}_{\text{farm},h}, \boldsymbol{x}_{\text{farm}}\right) + b = 0. \tag{34}$$

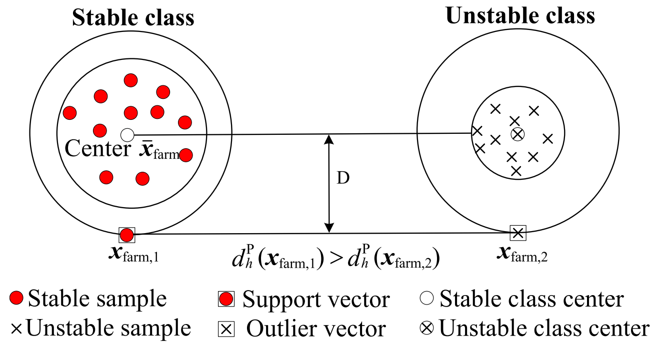

Fig. 4. Illustration of closeness of the samples.

D. Determination of Fuzzy Membership Function

The fuzzy membership variable s_h in (31) impacts the accuracy of the classification. The commonly used membership functions are based on the distance from the sample to the class center. The class center is typically chosen as the mean of the samples within the same class. However, this method does not take into account the closeness of the samples to each other. It cannot effectively distinguish between outlier vectors and support vectors. An example of the dense and sparse samples is shown in Fig. 4. In the illustrated case, $\boldsymbol{x}_{\text{farm},1}$ could possibly be a support vector, while $\boldsymbol{x}_{\text{farm},2}$ is more likely to be an outlier vector. The samples $\boldsymbol{x}_{\text{farm},1}$ and $\boldsymbol{x}_{\text{farm},2}$ have equal distance D to their respective class centers. Despite the equal distance, it is still not explicit which sample could be a support vector.

To select the support vector properly, this article proposes a membership function based on the weighted Mahalanobis distance. The Mahalanobis distance not only considers the distance from the sample to the class center, but also takes into account the distribution of the samples. To distinguish the influence of each parameter of the state variable $\boldsymbol{x}_{\text{farm}}$ on the stability boundary, the Relief-F algorithm is used to calculate the feature weights of each parameter, thereby improving the effect of classification.

1) Relief-F Feature Weighting: The Relief-F algorithm determines the importance of each parameter of the state variable $\boldsymbol{x}_{\text{farm}}$ to the stability boundary based on the differences in feature distances between similar and different class neighbors [25]. If a parameter has a small distance between similar class neighbors and a large distance difference between different class neighbors, this parameter is regarded to be beneficial for classification. Such a parameter is assigned a larger weight. Conversely, the weight of this feature is reduced.

For the state variable $\boldsymbol{x}_{\text{farm}}$ in (24) of the WPP, there are a total of $(M+1)$ parameters. The feature weights are defined as $\boldsymbol{W} = [W_1, \ldots, W_M, W_{M+1}]^{\text{T}}$. The calculation of feature weights requires n samplings in the stability index data. The ith sample is defined as $\boldsymbol{x}_{\text{farm},i}$. The initial value of $\boldsymbol{W}$ is set to 0. The feature weights are calculated with n iterations.

Considering ith sample $\boldsymbol{x}_{\text{farm},i}$ from the stability index data, the q nearest neighbor samples that belong to the same class with $\boldsymbol{x}_{\text{farm},i}$ are constructed as a set of $\{\boldsymbol{H}_j | j = 1, 2, \ldots, q\}$. Similarly, a total of q nearest neighbor samples from a different class of $\boldsymbol{x}_{\text{farm},i}$ is constructed as $\{\boldsymbol{M}_j | j = 1, 2, \ldots, q\}$. The class is defined as y, which represents either the same class or different classes. Relief-F algorithm supports more than one different classes. The feature weights of the ith iteration are calculated from the ith sample $\boldsymbol{x}_{\text{farm},i}$ as follows:

$$\boldsymbol{W}_i = \boldsymbol{W}_{i-1} - \frac{\sum_{j=1}^{q} e(\boldsymbol{x}_{\text{farm},i}, \boldsymbol{H}_j)}{nq} + \frac{\sum_{y \notin \text{class}(\boldsymbol{x}_{\text{farm},i})} \frac{p(y) \sum_{j=1}^{q} e(\boldsymbol{x}_{\text{farm},i}, \boldsymbol{M}_j)}{1 - p(\text{class}(\boldsymbol{x}_{\text{farm},i}))}}{nq} \tag{35}$$

where $p(y)$ represents the probability that a sample belongs to class y, $e(\boldsymbol{x}_{\text{farm},i}, \boldsymbol{H}_j)$ denotes the difference in features between sample $\boldsymbol{x}_{\text{farm},i}$ and sample $\boldsymbol{H}_j$. The difference in features is calculated as follows:

$$e(\boldsymbol{x}_{\text{farm},i}, \boldsymbol{H}_j) = \frac{|\boldsymbol{x}_{\text{farm},i} - \boldsymbol{H}_j|}{\max(\boldsymbol{x}_{\text{farm}}) - \min(\boldsymbol{x}_{\text{farm}})}. \tag{36}$$

With a total of n iterations, the feature weights $\boldsymbol{W}$ of the sample state variables are obtained by the Relief-F algorithm. The feature weight matrix $\boldsymbol{P}$ is constructed as follows:

$$\boldsymbol{P} = \text{diag}\{W_1, \ldots, W_M, W_{M+1}\}. \tag{37}$$

2) Weighted Mahalanobis Distance: The Mahalanobis distance is calculated based on the global information of the samples, representing the covariance distance of the data. This distance can effectively alleviate the interference of correlation among attributes, and it is independent of the measurement scale of the sample data, thus eliminating the effect of dimensions. Therefore, the Mahalanobis distance is especially applicable to the stability domain analysis of state variables with various dimensions in this study. The Mahalanobis distance between two arbitrary samples $\boldsymbol{x}_{\text{farm},1}$ and $\boldsymbol{x}_{\text{farm},2}$ is calculated as follows:

$$\begin{aligned} & d(\boldsymbol{x}_{\text{farm},1} - \boldsymbol{x}_{\text{farm},2}) \\ & \quad = \sqrt{(\boldsymbol{x}_{\text{farm},1}, \boldsymbol{x}_{\text{farm},2})^T \boldsymbol{S}^{-1} (\boldsymbol{x}_{\text{farm},1} - \boldsymbol{x}_{\text{farm},2})} \end{aligned} \tag{38}$$

where $\boldsymbol{S}$ is the total covariance matrix of the samples.

Further applying the feature weight matrix $\boldsymbol{P}$, the weighted Mahalanobis distance between the sample $\boldsymbol{x}_{\text{farm},h}$ and the class center $\bar{\boldsymbol{x}}_{\text{farm}}$ is calculated as follows:

$$\begin{aligned} & d_h^{\text{P}}(\boldsymbol{x}_{\text{farm},h}, \bar{\boldsymbol{x}}_{\text{farm}}, \boldsymbol{P}) \\ & \quad = \sqrt{(\boldsymbol{x}_{\text{farm},h} - \bar{\boldsymbol{x}}_{\text{farm}})^T (\boldsymbol{S} \cdot \boldsymbol{P})^{-1} (\boldsymbol{x}_{\text{farm},h} - \bar{\boldsymbol{x}}_{\text{farm}})}. \end{aligned} \tag{39}$$

The membership function based on the weighted Mahalanobis distance determines the importance of the sample according to the weighted Mahalanobis distance from the sample point to the center of its class. The smaller the distance, the greater the membership value assigned to the sample. The expression for the membership function based on the weighted Mahalanobis distance is as follows:

$$s_h = 1 - \frac{d_h^{\text{P}}(\boldsymbol{x}_{\text{farm},h}, \bar{\boldsymbol{x}}_{\text{farm}})}{r} \tag{40}$$

where $r = \max\{d_h^{\text{P}}(\boldsymbol{x}_{\text{farm},h}, \bar{\boldsymbol{x}}_{\text{farm}})\}$ represents class radius.

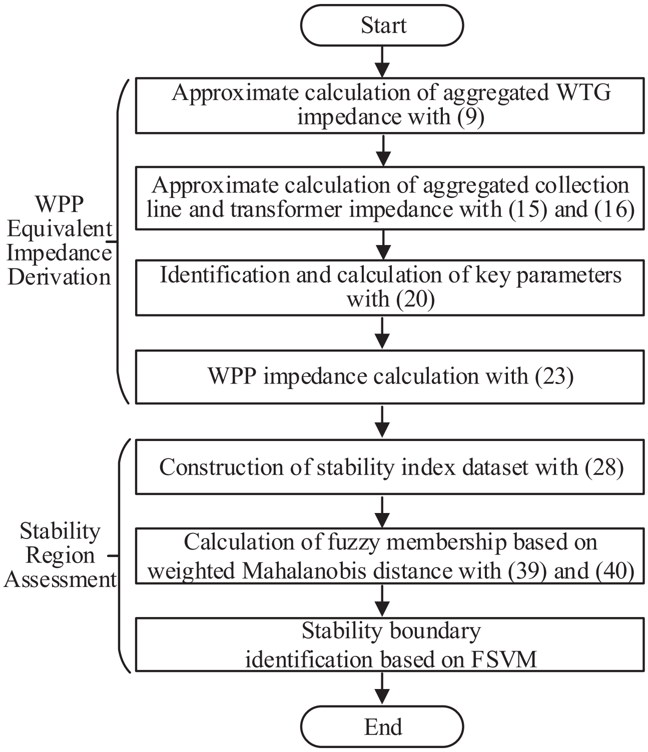

Fig. 5. Flowchart of the stability region assessment algorithm based on mechanism-data driven equivalent impedance.

E. Procedure of Stability Region Assessment Based on Mechanism-Data Driven Equivalent Impedance

The proposed stability region assessment algorithm based on mechanism-data-driven equivalent impedance is summarized in Fig. 5. This algorithm mainly consists of two parts: mechanism-data-driven equivalent impedance derivation and stability region assessment. First, the aggregated WTG impedance in each branch, as well as the aggregated collection line and transformer impedance, are approximately calculated with (9), (15), and (16). Second, the key parameters in the aggregated impedance of the WTG are identified with (20) to improve its accuracy. Then, the equivalent impedance of the WPP is formulated as (23) based on the aggregation of the equivalent impedance of each branch. After obtaining the equivalent impedance of the WPP, the dataset of relative stability can be generated with (28), and then the corresponding fuzzy membership of each sample point can be calculated with (40) based on weighted Mahalanobis distance with (39). Finally, the FSVM is used to identify the stability boundary, as given by (34).

V. CASE STUDY

The mechanism-data-driven aggregated impedance and the stability region of the WPP in Fig. 1 are verified. First, the aggregated impedance under diverse operating points is validated, showing the robustness of the aggregated impedance. Second, the stability region is established and validated for the active power of the WPP and the power distribution. Third, the stability enhancement by SVG is investigated by experimental platform.

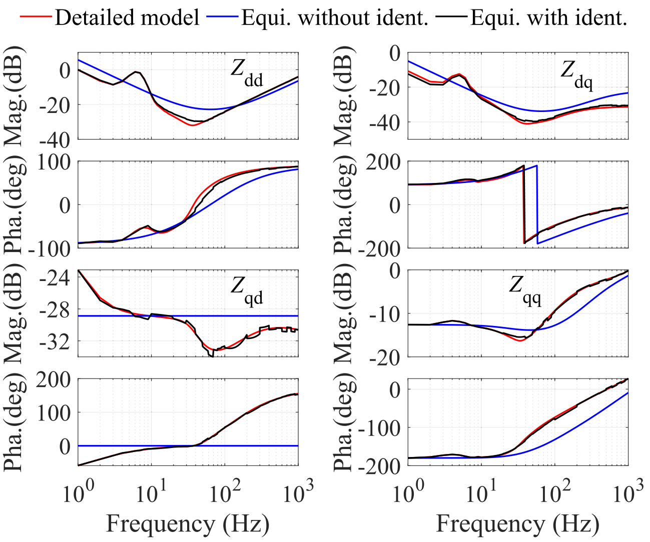

Fig. 6. Impedance comparison of branch 1 for detailed and aggregated model.

A. Verification of Mechanism-Data Driven Aggregated Impedance Under Diverse Operating Points

Referring to the WPP in Fig. 1, each branch has eight PMSGs. The active power of the PMSGs in a branch is set to 15 MW. The impedance obtained from the detailed model, the equivalent model without identification, and the equivalent model with identification are shown in Fig. 6. The results of the three models are labeled as “Detailed model,” “Equi. without ident.,” and “Equi. with ident.,” respectively. The equivalent model without identification shows a similar trend of impedance characteristics as that of the detailed model. However, obvious deviations of the magnitude and phase angle are observed at both low and high frequencies. To settle these deviations, it is necessary to identify impedance parameters with data-driven methods. With the proposed identification method of key parameters, the mechanism-data-driven aggregated impedance is highly consistent with that of the detailed model. The deviations are within $\pm 1\%$.

The aggregated impedance in Fig. 6 was validated at a given operating point. To verify robustness of the aggregation method, the next logical step is to validate performances under diverse operating points. The aggregated impedance of branch 1 at 10, 15, and 20 MW are verified in Fig. 7. Other branches are set to 15 MW. The SVG does not provide any reactive power. It is observed that the mechanism-data-driven aggregated model is of high accuracy at different operating points. The impedance of Z_{dd} and Z_{qd} remain unchanged with different active power. The magnitudes of Z_{dq} and Z_{qq} increase with increasing active power.

B. Verification of Stability Region of Active Power

The stability region of the active power P_{br1} of a single branch and the total active power P_{farm} of the WPP is established, as shown in Fig. 8. The stability region boundary is given by (34), which is determined with proposed FSVM. Taking into

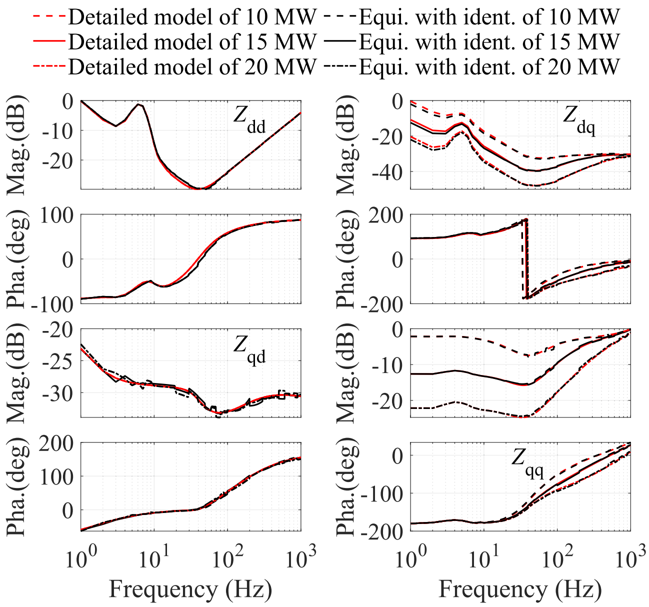

Fig. 7. Aggregated impedance of branch 1 at different operating points.

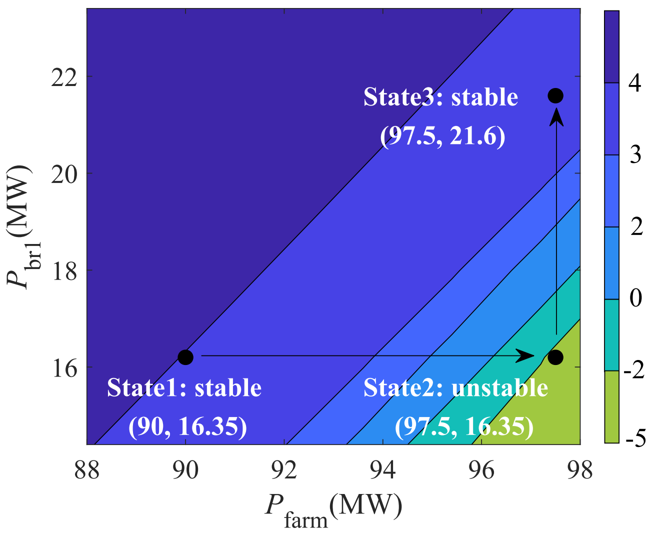

Fig. 8. Stability region of total power of WPP and active power of branch 1.

TABLE I
CHANGE IN ACTIVE POWER OPERATING POINT OF THE WPP

Operating state	P_{farm} (MW)	P_{br1} (MW)	Stability
state 1	90	16.35	stable
state 2	97.5	16.35	unstable
state 3	97.5	21.6	stable

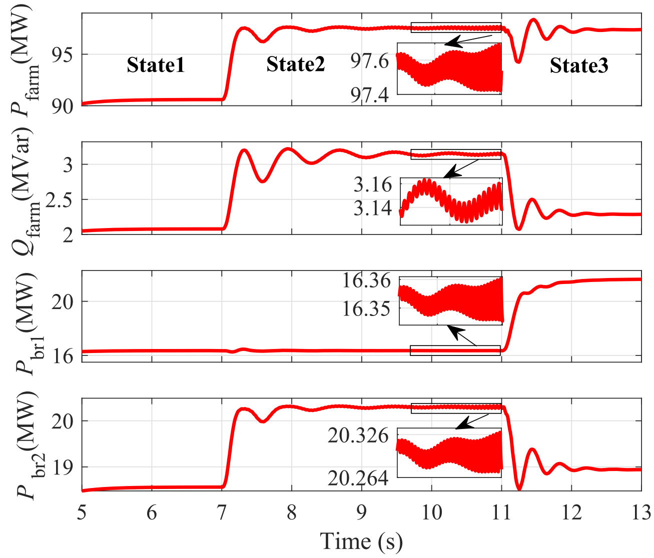

Fig. 9. Time-domain simulation to validate stability region of the active power of WPP and the active power of branch 1.

consideration the stability margin index M_{G} in (26), the stability region is indicated by gradient color.

The system operates initially in state 1, where the active power of the branch is $P_{\mathrm{br1}} = 16.35$ MW and the total active power of the WPP is $P_{\mathrm{farm}} = 90$ MW. The operating point in state 1 is located in a stable region where $M_{\mathrm{G}} > 0$. When the total active power P_{farm} increases to 97.5 MW, the system moves from state 1 to state 2. The active power of the branch 1 remains constant, while the active power of other branches increases proportionally. The system enters an unstable region where $M_{\mathrm{G}} < 0$. To improve the stability performance, the active power of the WPP is rearranged. The active power of the branch 1 is increased to $P_{\mathrm{br1}} = 21.6$ MW. The active power of the other branches decreases proportionally, while the total active power of the WPP remains unchanged. With the power redistribution inside the WPP, the system moves from state 2 to state 3, resulting in stable operation in state 3. The changes of the operating points of the WPP are summarized in Table I.

The proposed stability region in validated by the time-domain simulation, as shown in Fig. 9. The system operates stably in state 1. The total active power of the WPP increases at 7 s, resulting in unstable operations in state 2. The oscillations in P_{farm} and Q_{farm} of the WPP gradually increase, and P_{br1} and P_{br2} of individual branches diverge. It is noted that the power of other branches also diverge. To suppress the diverging oscillations, the active power of the branch 1 increases to 21.6 MW at 11 s. Simultaneously, the active power of other branches reduces to 18.9 MW. The oscillations are then damped in state 3. The time-domain results prove the effectiveness and accuracy of the stability region analysis in Fig. 8.

C. Stability Enhancement by Regulating Reactive Power With SVG

Considering the reactive power compensation of the SVG, the stability enhancement of the WPP is investigated. With the proposed stability region boundary in (34), the stability region for the active power P_{farm} of the WPP and the compensated reactive power Q_{SVG} of the SVG is shown in Fig. 10. For the given test system, a larger Q_{SVG} corresponds to a more stable operation. On the contrary, a larger P_{farm} tends to deteriorate

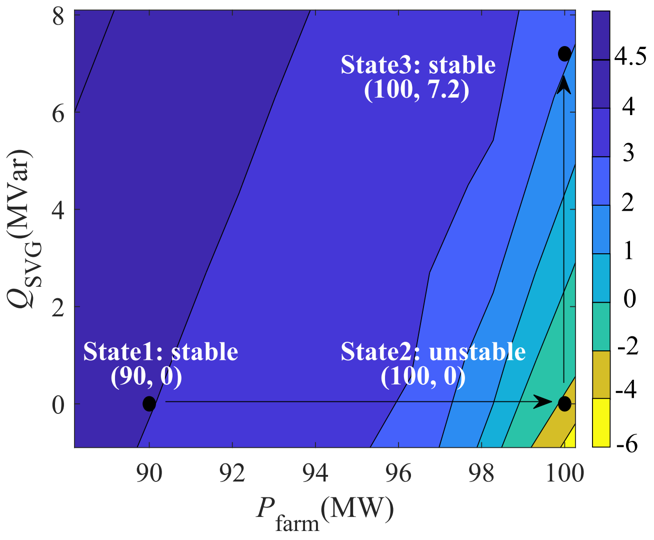

Fig. 10. Stability region of active power of WPP and reactive power of SVG.

TABLE II
CHANGE IN REACTIVE POWER OPERATING POINT OF THE SVG

Operating state	P_{farm} (MW)	Q_{SVG} (MVar)	Stability
state 1	90	0	stable
state 2	100	0	unstable
state 3	100	7.2	stable

stability. In state 1, the total active power of the WPP is $P_{\mathrm{farm}} = 90$ MW, and the reactive power of the SVG is zero. The operating point in the state 1 is located in a stable region, where $M_{\mathrm{G}} > 0$. In state 2, P_{farm} increases to 100 MW, and the increased active power is distributed equally to the WTGs. The SVG still does not provide any reactive power. The system moves into an unstable region since $M_{\mathrm{G}} < 0$ in state 2. To enhance the stability performance, the reactive power increases to 7.2 MVar, while the active power of the WPP is not changed. Then, the system moves into state 3. The system becomes stable since $M_{\mathrm{G}} > 0$. The changes in the reactive power operating point of the SVG are shown in Table II. It is shown that the proper regulation of the SVG could enhance stability performance.

The proposed stability region enhancement is validated by the controller-hardware-in-loop (CHIL) experimental platform, as shown in Fig. 11. The WPP is achieved at a real-time simulator RT-Lab 5700. The WTG power, the wind speed, and the WTG terminal voltage are transmitted to the edge computing device (ECD). Each branch is equipped with an ECD, and so is the SVG. The mechanism-data-driven aggregated impedance of the branch is performed at the ECDs. The online construction of the stability region is conducted in the center server, which is configured with an IntelÂ XeonÂ Gold 6230 processor. The stability region boundary is transferred to the wind farm controller (WFC). Whenever the system is approaching instability, the WFC issues a modified operating point of the WPP to RT-Lab. As such, the stability can be enhanced by regulating the operating point of the WPP in real time.

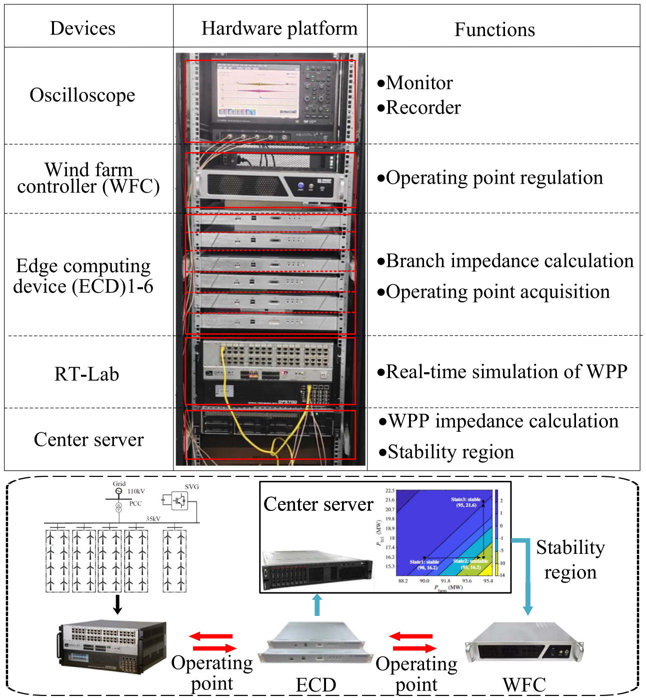

Fig. 11. Experimental platform of CHIL.

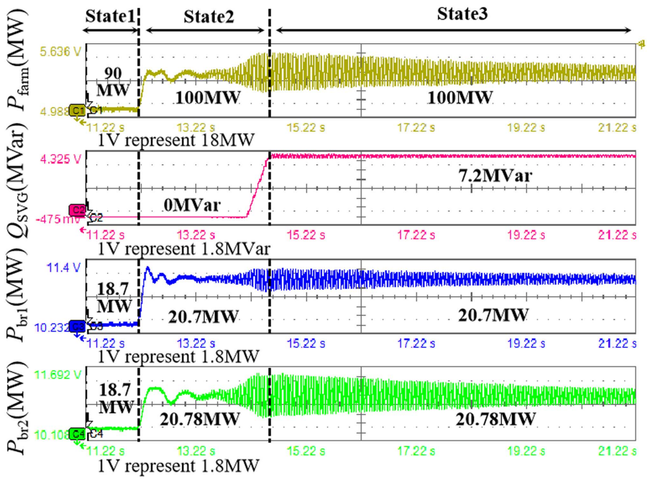

Fig. 12. Experimental results for stability enhancement by regulating reactive power of SVG.

The experimental results of stability region estimation and enhancement are shown in Fig. 12. The system is shown to be stable in the state 1, where $P_{\mathrm{farm}} = 90$ MW and $Q_{\mathrm{SVG}} = 0$ MVar. At the 12.1 s, the total active power of the WPP increases to $P_{\mathrm{farm}} = 100$ MW, resulting in unstable operation in state 2. The oscillation amplitude of the power gradually increases. To suppress the diverging oscillation, the reactive power of the SVG increases to 7.2 MVar at 14.1 s. The system then enters state 3, where the oscillation amplitude gradually decreases. The system operation enters a stable region. This confirms the results of the stability region in Fig. 12.

VI. Conclusion

Small-signal stability region assessment based on aggregated impedance is developed for the WPP equipped with PMSGs. The multiparameter stability region is estimated with high accuracy and efficiency.

The contributions of this article are threefold. First, the branch impedance is aggregated by combining parallel impedance calculation and key parameters modification. The mechanistic-data-driven method ensures the efficiency and accuracy of the equivalent impedance under different operating points, demonstrating its robustness. Second, based on the equivalent impedance and the stability margin indexes under different operating conditions, a stability region is developed using a supervised machine learning approach. The FSVM combing a weighted Mahalanobis distance significantly reduces the computation burden in stability model training, offering possibility for online applications. The proposed stability region includes a gradient boundary that evaluates the degree of relative stability. Third, based on the proposed stability region estimation, the stability margin could be enhanced by altering operating points. By adjusting the active power of the WPP and the reactive power of the SVG, the stability performance of the WPP is proven to be enhanced.

The methodology proposed in this article does not depend on a specific system architecture. It is not only applicable to WPPs with PMSG, but also to other grid-tied renewable energy systems, such as photovoltaic and energy storage systems.

Appendix

A. Impedance Model of Voltage Source Converter

The diagram of converter impedance is shown in Fig. 2. The filter impedance matrix $\boldsymbol{Z}_{\mathrm{g}}$ is given by

$$\boldsymbol{Z}_{\mathrm{g}} = \begin{bmatrix} R_{\mathrm{g}} + sL_{\mathrm{g}} & -\omega_{\mathrm{s}} L_{\mathrm{g}} \\ \omega_{\mathrm{s}} L_{\mathrm{g}} & R_{\mathrm{g}} + sL_{\mathrm{g}} \end{bmatrix} \tag{41}$$

where R_{g} and L_{g} are the filter resistance and inductance. The term $\boldsymbol{Z}_{\mathrm{gsc}}$ related to the inner current controller is given by

$$\boldsymbol{Z}_{\mathrm{gsc}} = \begin{bmatrix} -k_{\mathrm{p,i}} - k_{\mathrm{i,i}}/s & -\omega_{\mathrm{s}} L_{\mathrm{g}} \\ \omega_{\mathrm{s}} L_{\mathrm{g}} & -k_{\mathrm{p,i}} - k_{\mathrm{i,i}}/s \end{bmatrix} \tag{42}$$

where $k_{\mathrm{p,i}}$ and $k_{\mathrm{i,i}}$ are the coefficients of current controller. The transfer function Z_{PLL} of the PLL is given by

$$Z_{\mathrm{PLL}} = \frac{s k_{\mathrm{p,pll}} + k_{\mathrm{i,pll}}}{s^2 + s u_{\mathrm{sd}} k_{\mathrm{p,pll}} + u_{\mathrm{sd}} k_{\mathrm{i,pll}}} \tag{43}$$

where u_{sd} and u_{sq} are the PCC voltage where PLL is applied. With knowledge of the phase angle, the Park transformation $\boldsymbol{Z}_{\mathrm{ig}}$ for the current is given by

$$\boldsymbol{Z}_{\mathrm{ig}} = \begin{bmatrix} 0 & i_{\mathrm{gq}} Z_{\mathrm{PLL}} \\ 0 & -i_{\mathrm{gd}} Z_{\mathrm{PLL}} \end{bmatrix} \tag{44}$$

where i_{gd} and i_{gq} are the converter current in dq frame. The Park transformation $\boldsymbol{Z}_{\mathrm{ug}}$ for the voltage is given by

$$\boldsymbol{Z}_{\mathrm{ug}} = \begin{bmatrix} 0 & u_{\mathrm{gq}} Z_{\mathrm{PLL}} \\ 0 & -u_{\mathrm{gd}} Z_{\mathrm{PLL}} \end{bmatrix}. \tag{45}$$

The term $\boldsymbol{Z}_{\mathrm{ui}}$ related to the outer voltage and inner current controller is given by

$$\boldsymbol{Z}_{\mathrm{ui}} = \begin{bmatrix} (k_{\mathrm{p,udc}} + k_{\mathrm{i,udc}}/s)(k_{\mathrm{p,i}} + k_{\mathrm{i,i}}/s) & 0 \\ 0 & 0 \end{bmatrix}. \tag{46}$$

The terms $\boldsymbol{Z}_{\mathrm{cu}}$ and $\boldsymbol{Z}_{\mathrm{ci}}$ related to dc dynamics are given by

$$\boldsymbol{Z}_{\mathrm{cu}} = \begin{bmatrix} -3u_{\mathrm{gd}}/(4sC_{\mathrm{dc}}u_{\mathrm{dc}}) & -3u_{\mathrm{gq}}/(4sC_{\mathrm{dc}}u_{\mathrm{dc}}) \\ 0 & 0 \end{bmatrix} \tag{47}$$

$$\boldsymbol{Z}_{\mathrm{ci}} = \begin{bmatrix} -3i_{\mathrm{gd}}/(4sC_{\mathrm{dc}}u_{\mathrm{dc}}) & -3i_{\mathrm{gq}}/(4sC_{\mathrm{dc}}u_{\mathrm{dc}}) \\ 0 & 0 \end{bmatrix}. \tag{48}$$

References

[1] "RENEWABLE CAPACITY STATISTICS 2022," International Renewable Energy Agency (IRENA), 2022, ISBN-13:9789292604288.

[2] Y.-W. Kim and S.-K. Sul, "Stability analysis of active front end and permanent magnet synchronous generator with back EMF-Based sensorless control for DC marine vessels," *IEEE Trans. Power Electron.*, vol. 38, no. 4, pp. 5411–5421, Apr. 2023.

[3] B. Shao, S. Zhao, B. Gao, Y. Yang, and F. Blaabjerg, "Adequacy of the single-generator equivalent model for stability analysis in wind farms with VSC-HVDC systems," *IEEE Trans. Energy Convers.*, vol. 36, no. 2, pp. 907–918, Jun. 2021.

[4] P. Wang, Y. Ma, and H. Zhao, "Online assessment of multi-parameter stability region and stability margin of wind power plants," *Int. J. Elect. Power Energy Syst.*, vol. 155, 2024, Art. no. 109413.

[5] H. Gong, D. Yang, and X. Wang, "Impact analysis and mitigation of synchronization dynamics for dq impedance measurement," *IEEE Trans. Power Electron.*, vol. 34, no. 9, pp. 8797–8807, Sep. 2019.

[6] W. Dong, W. Du, X. Xie, and H. F. Wang, "An approximate aggregated impedance model of a grid-connected wind farm for the study of small-signal stability," *IEEE Trans. Power Syst.*, vol. 37, no. 5, pp. 3847–3861, Sep. 2022.

[7] T. Wang, S. Huang, M. Gao, and Z. Wang, "Adaptive extended Kalman filter based dynamic equivalent method of PMSG wind farm cluster," *IEEE Trans. Ind. Appl.*, vol. 57, no. 3, pp. 2908–2917, May/Jun. 2021.

[8] X. Wang, H. Yu, Y. Lin, Z. Zhang, and X. Gong, "Dynamic equivalent modeling for wind farms with DFIGs using the artificial bee colony with k-means algorithm," *IEEE Access*, vol. 8, pp. 173723–173731, 2020.

[9] N. Shabanikia, A. A. Nia, A. Tabesh, and S. A. Khajehoddin, "Weighted dynamic aggregation modeling of induction machine-based wind farms," *IEEE Trans. Sustain. Energy*, vol. 12, no. 3, pp. 1604–1614, Jul. 2021.

[10] W. Li, P. Chao, X. Liang, J. Ma, D. Xu, and X. Jin, "A practical equivalent method for DFIG wind farms," *IEEE Trans. Sustain. Energy*, vol. 9, no. 2, pp. 610–620, Apr. 2018.

[11] J. Zhang, M. Cui, and Y. He, "Robustness and adaptability analysis for equivalent model of doubly fed induction generator wind farm using measured data," *Appl. Energy*, vol. 261, 2020, Art. no. 114362.

[12] Y. Zhou, L. Zhao, and W.-J. Lee, "Robustness analysis of dynamic equivalent model of DFIG wind farm for stability study," *IEEE Trans. Ind. Appl.*, vol. 54, no. 6, pp. 5682–5690, Nov./Dec. 2018.

[13] Z. Zheng, Z. An, and C. Shen, "Evaluation method for equivalent models of PMSG-Based wind farms considering randomness," *IEEE Trans. Sustain. Energy*, vol. 10, no. 3, pp. 1565–1574, Jul. 2019.

[14] H. Zong, J. Lyu, X. Wang, C. Zhang, R. Zhang, and X. Cai, "Grey box aggregation modeling of wind farm for wideband oscillations analysis," *Appl. Energy*, vol. 283, p. 116035, Feb. 2021.

[15] Y. Hu, S. Bu, B. Zhou, Y. Liu, and C. W. Fei, "Impedance-based oscillatory stability analysis of high power electronics-penetrated power systems-a survey," *IEEE Access*, vol. 7, pp. 120774–120787, Aug. 2019.

[16] L. M. Halabi, I. M. Alsofyani, and K.-B. Lee, “Multi open-/short-circuit fault-tolerance using modified SVM technique for three-level HANPC converters,” *IEEE Trans. Power Electron.*, vol. 36, no. 12, pp. 13621–13633, Dec. 2021.

[17] M. Singh and A. G. Shaik, “Incipient fault detection in stator windings of an induction motor using Stockwell transform and SVM,” *IEEE Trans. Instrum. Meas.*, vol. 69, no. 12, pp. 9496–9504, Dec. 2020.

[18] A. Chen, D. Xie, D. Zhang, C. Gu, and K. Wang, “PI parameter tuning of converters for sub-synchronous interactions existing in grid-connected DFIG wind turbines,” *IEEE Trans. Power Electron.*, vol. 34, no. 7, pp. 6345–6355, Jul. 2019.

[19] M. Beza and M. Bongiorno, “On the risk for subsynchronous control interaction in type 4 based wind farms,” *IEEE Trans. Sustain. Energy*, vol. 10, no. 3, pp. 1410–1418, Jul. 2019.

[20] B. Wen, D. Boroyevich, R. Burgos, P. Mattavelli, and Z. Shen, “Analysis of D-Q small-signal impedance of grid-tied inverters,” *IEEE Trans. Power Electron.*, vol. 31, no. 1, pp. 675–687, Jan. 2016.

[21] P.-H. Huang, M. S. El Moursi, W. Xiao, and J. L. Kirtley, “Subsynchronous resonance mitigation for series-compensated DFIG-based wind farm by using two-degree-of-freedom control strategy,” *IEEE Trans. Power Syst.*, vol. 30, no. 3, pp. 1442–1454, May 2015.

[22] H. Liu, X. Xie, C. Zhang, Y. Li, H. Liu, and Y. Hu, “Quantitative SSR analysis of series-compensated DFIG-Based wind farms using aggregated RLC circuit model,” *IEEE Trans. Power Syst.*, vol. 32, no. 1, pp. 474–483, Jan. 2017.

[23] J. Liu, W. Yao, J. Fang, J. Wen, and S. Cheng, “Stability analysis and energy storage-based solution of wind farm during low voltage ride through,” *Int. J. Electr. Power Energy Syst.*, vol. 101, pp. 75–84, Oct. 2018.

[24] B. Chen, Y. Fan, W. Lan, J. Liu, C. Cao, and Y. Gao, “Fuzzy support vector machine with graph for classifying imbalanced datasets,” *Neurocomputing*, vol. 514, pp. 296–312, Dec. 2022.

[25] R. J. Urbanowicz, M. Meeker, W. La Cava, R. S. Olson, and J. H. Moore, “Relief-based feature selection: Introduction and review,” *J. Biomed. Inform.*, vol. 85, pp. 189–203, 2018.

Shiyao Qin was born in Shanxi, China, in 1977. He received the M.E. degree in electrical engineering from the Taiyuan University of Technology, Taiyuan, China, in 2002, and the Ph.D. degree in electrical engineering from Southeast University, Nanjing, China, in 2021.

He is currently with the China Electric Power Research Institute, Beijing, China, and is a university-enterprise-appointed Changjiang Scholar with Shandong University, Jinan, China. His research interests include renewable energy grid-connected operation and control technology.

Peng Wang (Member, IEEE) was born in Shandong, China, in 1988. He received M.E. degree in electrical engineering from Shandong University, China, in 2014, and the the Dr.-Ing. (*summa cum laude*) degree in electrical engineering from Technical University of Berlin, Berlin, Germany, in 2020.

He is currently with the School of Electrical Engineering, Shandong University. In 2018, he was an Electrical Engineer with State Grid Corporation of China, Beijing, China. His research interests include modeling and stability analysis of ac–dc power system integrated with renewable generation.

Shaolin Li was born in Shaanxi, China, in 1984. He received the M.E. and Ph.D. degrees in electrical engineering from the Hefei University of Technology, Hefei, China, in 2010 and 2022, respectively.

He is currently with the China Electric Power Research Institute, Beijing, China. His research interests include wind power grid-connected simulation, control, and test evaluation technology.

Haoran Zhao (Senior Member, IEEE) received the B.E. degree in electrical engineering and automation from Shandong University, Jinan, China, in 2005, the M.E. degree in electrical engineering and automation from the Technical University of Berlin, Berlin, Germany, in 2009, and the Ph.D. degree in electrical engineering from the Technical University of Denmark, Kongens Lyngby, Denmark, in 2015.

He is a Postdoctoral with the Center for Electric Technology, Technical University of Denmark. In 2015, he was an Electrical Engineer with State Grid Corporation of China, Beijing, China. From 2010 to 2011, he was an Application Developer with DIgSILENT GmbH, Gomaringen, Germany. His research interests include modeling and integration study of wind power, control of energy storage systems, and voltage stability analysis.

Jinlong Wang received the B.S. and M.S. degrees in electrical engineering from Shandong University, Jinan, China, in 2019 and 2022, respectively. He is currently working toward the Ph.D. degree in electrical engineering with Shandong University.

His research interests include modeling and control of power electronics and stability analysis of power electronics-based power systems.

Jia Luo received the B.S. degree from the Huazhong University of Science and Technology, Wuhan, China, in 2015, and the M.S. degree from Shandong University, Jinan, China, in 2020, both in electrical engineering. He is currently working toward the Ph.D. degree in electrical engineering with Shandong University.

His research interests include modeling and control of DFIG, LVRT strategy of DFIG, and voltage stability analysis.